Deriving Models of Cartilaginous Cells From Confocal Fluorescence Microscopy Images to Estimate Dielectric Properties

Vien Lam Che[1], Julius Zimmermann[1], Yilu Zhou[2], X. Lucas Lu[2], and Ursula van Rienen[1,3,4]

[1]Institute of General Electrical Engineering, University of Rostock, 18059 Rostock, Germany
[2]Department of Mechanical Engineering, University of Delaware, Delaware, DE 19716 USA
[3]Department Life, Light and Matter, University of Rostock, 18059 Rostock, Germany
[4]Department of Ageing of Individuals and Society, Interdisciplinary Faculty, University of Rostock, 18051 Rostock, Germany

The dielectric properties of cartilage are essential for the development of reliable numerical models of electrical stimulation devices intended for the regeneration of cartilage. They are, however, not widely known. To determine the dielectric properties of cartilage, we propose a numerical workflow that incorporates detailed tissue-specific 3-D geometries based on fluorescent microscopic images and describes how different parameters can affect the results. We investigated a typical bioimpedance setup that can be used for impedance sensing and electrical stimulation. The obtained results provided valuable insights that can aid in the design and implementation of future experiments, ensuring their accuracy and reliability.

Index Terms— **Bioimpedance, computational electromagnetics, electrical stimulation, numerical models.**

I. Introduction

RESEARCH on electrical stimulation for cartilage regeneration is growing over time. Numerical simulations can pave the way for gaining insights into an interaction between cells and an electric field. In this context, the dielectric properties of biological tissue are one of the key components. However, those properties of cartilage in Hz and kHz range are not experimentally well known leading to challenges in the generation of reliable and robust numerical models. The permittivity and conductivity values at these intermediate frequencies are usually retrieved from a parametric model, which has been argued to be ambiguous [1]. For estimating dielectric properties, fine-grained numerical models have emerged as a potential solution [2], [3]. In previous works, artificial geometries based on a stochastic geometrical tissue model have been used. Here, we improve on that by deriving geometry models from cell images, thus reflecting realistic cell distributions. Furthermore, we cover more realistic cell shapes and include cell organelles. Hence, we determine the dielectric properties of cartilage by employing more realistic and complex geometrical models than in previous works. The effects of distinct input parameters are also investigated in the models using uncertainty quantification (UQ) and sensitivity analysis. Finally, we study the cell-based approach on a realistic electrode as used in electric cell–substrate impedance sensing (ECIS). With ECIS chips, processes such as cell growth, migration, adhesion, and proliferation can be studied in cell experiments on hydrogels, bone, and cartilage [4]. Our modeling approach and its results can be employed to develop precise future experiments.

Manuscript received 10 June 2023; revised 7 August 2023; accepted 16 August 2023. Date of publication 21 August 2023; date of current version 27 February 2024. Corresponding author: U. van Rienen (e-mail: ursula.van-rienen@uni-rostock.de).

Color versions of one or more figures in this article are available at https://doi.org/10.1109/TMAG.2023.3307009.

Digital Object Identifier 10.1109/TMAG.2023.3307009

II. Materials and Methods

A. Mesh Generation Workflow

1) Image Segmentation: In this study, meshes were generated from cellular geometries identified from confocal microscope (Zeiss LSM510) images. The image acquisition and benchmark cell volume are described elsewhere [5]. We simplified the geometric description of the cells by fitting ellipsoids to the contiguous set of voxels affiliated with each cell to determine their location, radii, and orientations within the tissue using *ImageJ* v.1.53f51 [6]. To mitigate the challenge of adjacent cell separation in the z-direction caused by anisotropic voxel size, the 3-D images were resampled to obtain isotropic voxels. Various filters were then applied to reduce image noise, enhance the image contrast, and subtract the background due to uneven illumination. Thereafter, an auto threshold technique is utilized to segment images into cell interior and exterior. Large artifactual objects with an area exceeding 300 μm^2 were removed from the image slices. Tiny noises and artifacts cannot be filtered based on this criterion as parts of the cells could be removed from individual image slices. Instead, a volume filter from *BoneJ2* v.7.0.13 [7] was applied to remove various small noises with a volume of less than 200 μm^3. Subsequently, holes were filled and touching cells were separated or small cell parts were connected based on the *Distance Transform Watershed* algorithm [8]. Finally, *3-D ellipsoid fitting* [9] was employed. The entire procedure was wrapped into an *ImageJ* script to perform batch processing of all images.

2) Defining the Geometric Input: The characteristic dimensions of the ellipsoids were stored in input files formatted consistently with previous research [10]. As each image was recorded for only one particular cartilage zone, a combination of different zones was applied for the geometrical model of the sample utilized in this study. Furthermore, we added a pericellular matrix (PCM) with a thickness of 2.5, 3.6,

and 3 μm in the superficial, middle, and deep zones, respectively [11]. The cell nucleus was modeled by scaling the cell to 80% of its volume. Four cell geometry scenarios were utilized to determine the dielectric properties of the tissue. The single-shell (SS) model includes only the cells and their membranes. The single-shell-wall (SSW) geometry comprises the cells, their membranes and their PCM. The double-shell (DS) geometry contains the cells, their membranes, the cell nucleus envelopes and the nucleus. The double-shell-wall (DSW) geometry consists of the same components as the DS but has the PCM in addition.

3) Mesh Generation: We used *NGSolve* [12] with the mesh generator *Netgen* to generate the geometry in an automated manner. From the geometries, we generated quality meshes using a predefined mesh hypothesis. We ensured that the mesh had a surface and volume error of less than 1% with respect to the cell surface area and volume. A second-order finite element method (FEM) with curved elements was applied.

B. Numerical Modeling

Magnetic fields and eddy currents can be assumed negligibly small, so that we could solve the electro-quasistatic (EQS) [13] field equation as follows:

$$\nabla \cdot [(\sigma + j\omega\epsilon)\nabla\phi] = 0 \tag{1}$$

where ϕ is the electric potential, σ is the conductivity, ε is the permittivity, and ω is the angular frequency. The impedance Z of the considered sample can be determined from the solution of (1) using the instantaneous power dissipation P [2]. The complex permittivity $\hat{\varepsilon}$ can be computed using the relation given below:

$$Z = \frac{1}{j\omega\hat{\epsilon}C_0} \tag{2}$$

with the unit capacitance C_0 [1]. Then, σ and ε can be derived from $\hat{\varepsilon} = \varepsilon - j\sigma/\omega$. A voltage drop of 1 V was applied to the top and the bottom of the extracellular matrix (ECM) region, thus creating a parallel-plate capacitor-like electrode configuration. Simulated frequencies ranged from 1 kHz to 1 THz with 10 logarithmically spaced points per decade. Due to the thinness of membranes and nucleus envelopes, we used a thin layer approximation [3], [14]. The FEM was used to solve (1) using a conjugate orthogonal conjugate gradient (COCG) solver with a Jacobi preconditioner in *NGSolve*. The correctness of the numerically computed impedance was checked with a linear Kramers–Kronig validity test [15] and analytical solutions for a spherical cell, implemented in *ImpedanceFitter* [16], [2].

First, the UQ analysis of the DSW model was conducted on the inexpensive analytical model using 10^5 samples for the quasi-Monte Carlo sampling by employing the *Uncertainpy* toolbox [17]. Then, only the most relevant parameters were employed to examine the expensive numerical model using polynomial chaos expansion with the order of four. The 90% percentile prediction intervals and the first-order Sobol indices were calculated. Given the UQ results obtained from the analytical solution, the importance of parameters can be determined by examining their Sobol indices. The most important parameters were selected if their frequency-dependent Sobol indices exceeded 0.2. Table I gives an overview of all possible hypotheses in the UQ analysis. Due to the lack of biological measurement data, we analyzed only uniform distributions as they reflect our knowledge regarding the uncertainties of the individual parameters. All the computations were conducted using parallel computing on the HAUMEA high-performance computing (HPC) cluster of the University of Rostock (each node equipped with 2 Intel Xeon Gold 6248 40-core CPUs and 192 GB RAM).

In this work, besides using a simplistic parallel-plate capacitor geometry to apply the electric fields, we considered the ECIS chip as a bioimpedance application. A simplified geometry of one cell culture well with interdigitated electrodes was constructed, as illustrated in Fig. 1. The cells were arranged on the electrode surface by replicating the original cell block obtained from the confocal microscopy image, ensuring complete coverage of the entire electrode area. All dimensions of the ECIS geometry are given in Fig. 1. Again, a voltage drop of 1 V was applied across the electrodes. The more complex geometry required a high amount of memory not available on the HPC cluster. One reason was the computer-aided design (CAD) kernel in *Netgen*, which allocated a few hundred GB of memory for the complex geometry. As the geometry is required on every processor to curve the mesh, we used shared-memory parallelization on a server featuring two AMD EPYC 7H12 64-core CPUs with 4 TB RAM.

TABLE I

MODEL PARAMETERS FOR UQ OF THE ANALYTICAL SOLUTION OF THE DSW MODEL GIVEN IN TERMS OF THE UNIFORM DISTRIBUTION $\mathcal{U}$. σ: CONDUCTIVITY, ε: RELATIVE PERMITTIVITY; SUBSCRIPT: m CELL MEMBRANE, CYT: CYTOPLASM, w: PERICELLULAR LAYER, NE: NUCLEAR ENVELOPE, NP: NUCLEOPLASM

Parameter	Distribution	Reasoning	Base case
ε_{m}	$\mathcal{U}(1.4, 16.8)$	[18]	5.8
σ_{m} / S m^{-1}	$\mathcal{U}(8 \cdot 10^{-8}, 5.6 \cdot 10^{-5})$	[18]	$8.7 \cdot 10^{-6}$
σ_{cyt} / S m^{-1}	$\mathcal{U}(0.033, 1.1)$	[18]	0.48
$\varepsilon_{\mathrm{cyt}}$	$\mathcal{U}(60, 77)$	[18]	60
d_{m} / nm	$\mathcal{U}(3.5, 10.5)$	[18]	7
d_{n} / nm	$\mathcal{U}(20, 60)$	[18]	40
d_{w} / μm	$\mathcal{U}(2, 4)$	[11]	see II-A2
σ_{ne} / S m^{-1}	$\mathcal{U}(8.3 \cdot 10^{-7}, 7 \cdot 10^{-3})$	[18]	$3 \cdot 10^{-3}$
$\varepsilon_{\mathrm{ne}}$	$\mathcal{U}(6.8, 100)$	[18]	41
σ_{np} / S m^{-1}	$\mathcal{U}(0.25, 2.2)$	[18]	0.95
$\varepsilon_{\mathrm{np}}$	$\mathcal{U}(32, 300)$	[18]	120
σ_{wall} / S m^{-1}	$\mathcal{U}(0.005, 0.1)$	Guess	0.01
$\varepsilon_{\mathrm{wall}}$	$\mathcal{U}(10, 50)$	Guess	20

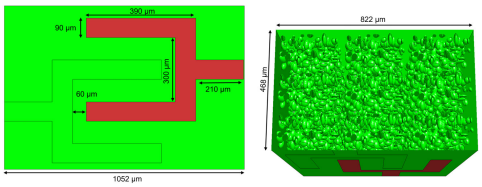

Fig. 1. Left: Bottom view of the simplistic ECIS chip, including two interdigitated electrodes with two fingers per electrode. Right: Clipped geometry, including the DSW model of the cells on top of the electrodes.

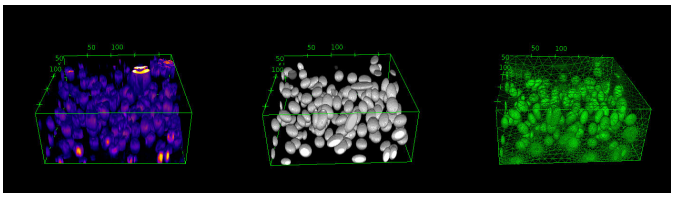

Fig. 2. From left to right: 3-D view of the original image of the deep zone, the fit ellipsoids and the mesh created with *Netgen*. The unit of the specified lengths is μm.

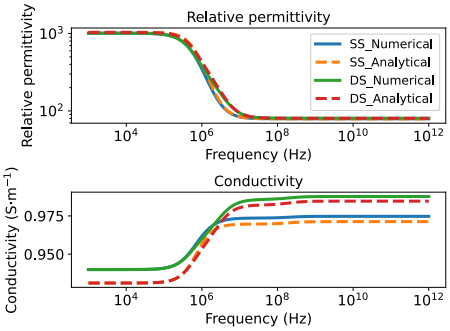

Fig. 3. Numerically computed dielectric properties for different geometry models in which three cartilaginous zones were combined using parallel plate capacitor electrodes with the parameter given in the base case in Table I. The total number of cells is 537.

III. Results and Discussion

After the ellipsoidal fitting, an average cell volume is $2157 \pm 957\ \mu\text{m}^3$, which is in good agreement with the reported value in [5]. This indicates a reliable segmentation process. Moreover, the mesh can preserve the cells' volume, orientation, and position as depicted in the original microscopic image (example in Fig. 2). The mesh of the DS model led to the highest global DOFs ($\approx 50 \times 10^6$). The numerically computed curves and analytical estimates of all models are relatively similar (not shown). For all models, the conductivity at low frequencies did not exhibit a frequency dependence and a β-dispersion appears between 100 kHz and 1 MHz (Fig. 3). By including the PCM and cell nucleus, a γ-dispersion (10 MHz to 1 GHz) could be modeled. According to our assumption, this dispersion is more closely associated with the PCM than with the cell nucleus. A reduction in conductivity occurs with the addition of the PCM, whereas it increases when including the nucleus. Thus, simple models do not serve well for analyzing the dielectric behavior of a tissue, where the internal layers differ from the external layers.

Based on the UQ of the analytical solution, out of the input parameters, four parameters exhibited the most significant influence on the computed dielectric properties, namely ε_{np}, σ_{wall}, $\varepsilon_{\text{wall}}$, and ε_m. Those parameters resulted in 142 FEM simulations, and each simulation with $\approx 40 \times 10^6$ DOFs took more than 1 h. The UQ analysis of the numerical model was completed within approximately two days. The 90% prediction interval of the computed conductivity varies around 1% from its mean value (Fig. 4). While the 90% prediction interval of the calculated relative permittivity initially ranges from about 400 to 2700, it drastically narrows at around 10 MHz. Up to 1 GHz, the tissue conductivity mainly depends on the

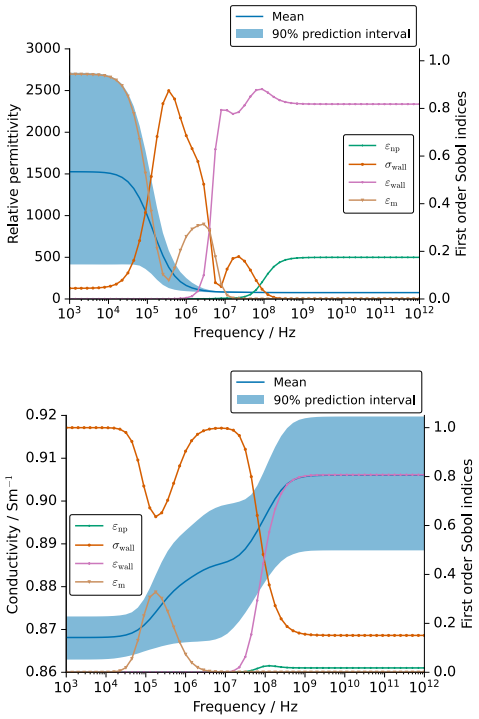

Fig. 4. Mean value and 90% prediction interval of the relative permittivity and the conductivity from the UQ analysis of the DSW model are demonstrated over a frequency range with the parameters given in Table I.

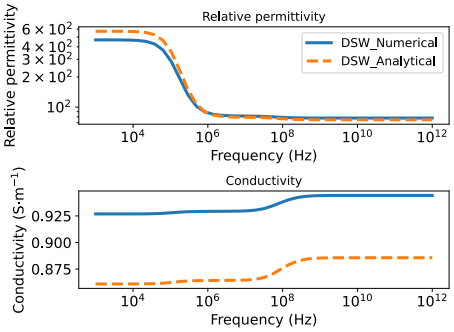

Fig. 5. Numerically and analytically computed dielectric properties for DSW models using the ECIS chip with the parameters given in the base case in Table I. The geometry contains 6300 cells.

conductivity of the PCM. Beyond the γ-dispersion, the relative permittivity of the PCM has the most significant impact on the computed conductivity. The permittivity of the membrane predominantly affects the relative permittivity of cartilage at low frequencies. In the range of the β-dispersion and γ-dispersion, the estimated permittivity is primarily influenced by the conductivity of the PCM. Above 10 MHz, the PCM relative permittivity accounts for the most considerable impact on the estimated permittivity, but the variation of the tissue permittivity is minimal.

The ECIS chip geometry, comprising 6300 cells, led to $\approx 80 \times 10^6$ DOFs, requiring approximately one day for meshing. The computational simulation took almost five days to complete. As depicted in Fig. 5, the numerical model's conductivity is higher than the one computed from the analytical solution. This disparity arises due to the assumption

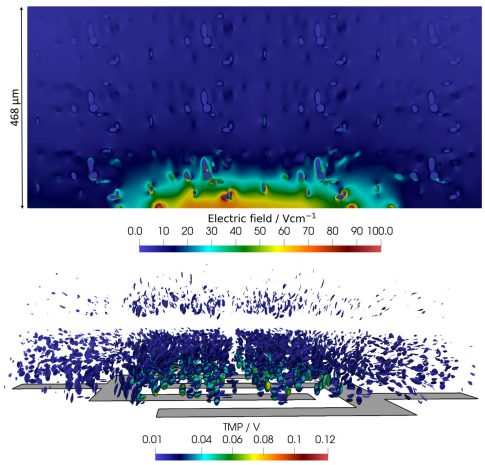

Fig. 6. Top: Electric field distribution in the cross section through the central YZ-plane at 1 kHz with the parameters used for the base case in Table I. For a more insightful visualization, the electric field strength was set to a maximum of 100 V cm^{-1}; the actual maximum field strength is around 220 V cm^{-1}. Bottom: Stimulated domain where the absolute TMP value is higher than 0.01 V. Only the cells positioned roughly 200 μm above the electrode can be stimulated.

made in the analytical solution, which considers the entire domain exposed to an external homogeneous field. In contrast, the ECIS chip produces an inhomogeneous field, with the electric field reaching only a few tens of micrometers above the electrode. This limited exposure of the volume to the field and the gap between the electrodes and the cells lead to a more conductive domain under electrical stimulation, resulting in higher conductivity and lower permittivity. Besides impedance spectroscopy, our approach allows for the investigation of electrical stimulation in cartilage regeneration. For instance, we can obtain the transmembrane potential (TMP) as a measure of stimulation. From Fig. 6, it is evident that the limited penetration of the electric field results in a vanishing TMP for cells near the top of the domain. Consequently, a reduced model can be employed to simulate only the stimulated domain, significantly reducing the computational effort. The computational cost is currently the main bottleneck of the approach. In particular, the mesh generation of complex geometries is time consuming and error prone. We also encountered that mesh-partitioning algorithms failed, which prevented significantly faster, distributed computing approaches on the HPC cluster. Future research will focus on these aspects to further leverage scalable HPC techniques.

IV. Conclusion

In sum, our automatic numerical workflow enables the estimation of dielectric properties using detailed tissue-specific 3-D geometries derived from fluorescent images. Our findings shed light on the factors influencing the dielectric properties of cartilaginous tissue across various frequency ranges. Additionally, we have successfully demonstrated the feasibility of modeling ECIS chips together with detailed cell models. In future research, integrating numerical models of electrical stimulation with impedance measurements will enable the development of a "digital twin" framework [19]. The digital twin relies on feedback between the numerical model and experimental data. Ultimately, these advancements will pave the way for live monitoring and controlled electrical stimulation approaches in patient care.

Acknowledgment

This work was supported by the Deutsche Forschungsgemeinschaft (DFG, German Research Foundation) under Grant SFB 1270/1,2 - 299150580.

References

[1] J. Zimmermann and U. van Rienen, "Ambiguity in the interpretation of the low-frequency dielectric properties of biological tissues," *Bioelectrochemistry*, vol. 140, Aug. 2021, Art. no. 107773.

[2] J. Zimmermann, L. V. Che, and U. van Rienen, "Using tissue-specific numerical models to estimate the dielectric properties of cartilage," in *Proc. Int. Workshop Impedance Spectrosc. (IWIS)*, Sep. 2022, pp. 28–32.

[3] J. Zimmermann, "Numerical modelling of electrical stimulation for cartilage tissue engineering," Ph.D. dissertation, Dept. Comput. Sci. Elect. Eng., Univ. Rostock, 2022, doi: 10.18453/rosdok_id00004117.

[4] R. Szulcek, H. J. Bogaard, and G. P. V. N. Amerongen, "Electric cell-substrate impedance sensing for the quantification of endothelial proliferation, barrier function, and motility," *J. Visualized Exp.*, no. 85, Mar. 2014, Art. no. e51300.

[5] M. Lv et al., "Identification of chondrocyte genes and signaling pathways in response to acute joint inflammation," *Sci. Rep.*, vol. 9, no. 1, p. 93, Jan. 2019.

[6] C. A. Schneider, W. S. Rasband, and K. W. Eliceiri, "NIH image to ImageJ: 25 years of image analysis," *Nature Methods*, vol. 9, no. 7, pp. 671–675, Jul. 2012.

[7] R. Domander, A. A. Felder, and M. Doube, "BoneJ2—Refactoring established research software," *Wellcome Open Res*, vol. 6, p. 37, Apr. 2021.

[8] D. Legland, I. Arganda-Carreras, and P. Andrey, "MorphoLibJ: Integrated library and plugins for mathematical morphology with ImageJ," *Bioinformatics*, vol. 32, no. 22, pp. 3532–3534, Nov. 2016.

[9] J. Ollion, J. Cochennec, F. Loll, C. Escudé, and T. Boudier, "TANGO: A generic tool for high-throughput 3D image analysis for studying nuclear organization," *Bioinformatics*, vol. 29, no. 14, pp. 1840–1841, Jul. 2013.

[10] C. J. Bennetts, S. Sibole, and A. Erdemir, "Automated generation of tissue-specific three-dimensional finite element meshes containing ellipsoidal cellular inclusions," *Comput. Methods Biomechanics Biomed. Eng.*, vol. 18, no. 12, pp. 1293–1304, Sep. 2015.

[11] P. Julkunen, W. Wilson, J. S. Jurvelin, and R. K. Korhonen, "Composition of the pericellular matrix modulates the deformation behaviour of chondrocytes in articular cartilage under static loading," *Med. Biol. Eng. Comput.*, vol. 47, no. 12, pp. 1281–1290, Dec. 2009.

[12] J. Schöberl, "C++ 11 implementation of finite elements in NGSolve," *Inst. Anal. Sci. Comput., Vienna Univ. Technol.*, vol. 30, Sep. 2014.

[13] U. van Rienen et al., "Electro-quasistatic simulations in bio-systems engineering and medical engineering," *Adv. Radio Sci.*, vol. 3, pp. 39–49, May 2005.

[14] G. Pucihar, T. Kotnik, B. Valič, and D. Miklavčic, "Numerical determination of transmembrane voltage induced on irregularly shaped cells," *Ann. Biomed. Eng.*, vol. 34, no. 4, pp. 642–652, Mar. 2006.

[15] M. Schönleber, D. Klotz, and E. Ivers-Tiffée, "A method for improving the robustness of linear Kramers–Kronig validity tests," *Electrochimica Acta*, vol. 131, pp. 20–27, Jun. 2014.

[16] J. Zimmermann and L. Thiele, "j-zimmermann/ImpedanceFitter: v2.0.2," Chair Electromagn. Field Theory, Inst. Gen. Elect. Eng., Univ. Rostock, Rostock, Germany, 2021, doi: 10.5281/zenodo.5116618.

[17] S. Tennøe, G. Halnes, and G. T. Einevoll, "Uncertainpy: A Python toolbox for uncertainty quantification and sensitivity analysis in computational neuroscience," *Frontiers Neuroinform.*, vol. 12, p. 49, Aug. 2018.

[18] I. Ermolina, Y. Polevaya, and Y. Feldman, "Analysis of dielectric spectra of eukaryotic cells by computer modeling," *Eur. Biophys. J.*, vol. 29, no. 2, pp. 141–145, May 2000.

[19] J. Zimmermann et al., "Using a digital twin of an electrical stimulation device to monitor and control the electrical stimulation of cells in vitro," *Frontiers Bioeng. Biotechnol.*, vol. 9, Dec. 2021, Art. no. 765516.